Thermomechanical and calorimetric characterization of crack tip zones under large heterogeneous deformations, Part I: A method coupling full kinematic and thermal fields for high resolution surface micro-calorimetry

J. Trubert, J. -B. Le Cam, S. Charles, R. Fernandes, V. Lemos

Polymer 342 (2026) 129286

Contents lists available at ScienceDirect

Polymer

journal homepage: www.elsevier.com/locate/polymer

Thermomechanical and calorimetric characterization of crack tip zones under large heterogeneous deformations, Part I: A method coupling full kinematic and thermal fields for high resolution surface micro-calorimetry

J. Trubert, J.-B. Le Cam *, S. Charlès, R. Fernandes, V. Lemos

Université de Rennes, Institut de Physique de Rennes, UMR 6251 CNRS/Université de Rennes, Campus de Beaulieu, Bât. 10B, 35042 Rennes Cedex, France

ARTICLE INFO

Keywords:
High resolution surface calorimetry
Large strains
Coupled visible and IR images

ABSTRACT

The thermomechanical and calorimetric responses accompanying the deformation of materials bring complementary information to purely mechanical approaches. In the case of elastomers, many studies carried out under homogeneous strain fields are available in the recent literature. They enable us to discuss the nature of the elasticity (due entropic and/or isentropic couplings), to identify the intrinsic dissipation (due to viscosity and/or damage) and to determine whether or not the material experiences microstructure changes. In the case large heterogeneous strain fields, typically those induced in the vicinity of a crack tip, imaging systems must be coupled in order to track the points that are moving the IR images. The first part of the present article deals with the development of a methodology for reconstructing heat source surface fields in the case of large heterogeneous deformations. This methodology is based on the coupling of full kinematic and thermal fields measurements, for compensating the point motion in the thermal images in order to calculate the heat source from the heat diffusion equation. A complete metrological characterization has been carried out. It shows that the compensation technique does not alter significantly the thermal resolution in the variation range of experimental parameters in relation with the experimental setup used. The heat source resolution reached is less than 5 10^3 W/m^3, which is two orders of magnitude less than the heat source values classically measured for stretched elastomers. The accuracy of the conduction term has been evaluated in the Lagrangian configuration according to the temperature gradient level. This methodology is used in the second part of the present paper to characterize full strain, calorimetric and strain-induced crystallinity fields at the crack tip of a natural rubber submitted to cyclic loadings.

1. Introduction

The calorimetric response accompanying the deformation of materials provides information of importance to better understand and model the physical phenomena involved. This response is obtained by using a temperature measurement and by applying a simplification of the heat diffusion equation formulation for determining the corresponding heat power density. Contrarily to the temperature, the heat power density, also referred to as the heat source in many studies, is an intrinsic quantity to investigate the thermomechanical behavior in the sense that it does not depend on conducto-convective effects [1,2]. In the case of elastomeric materials, characterizing the calorimetric response enables us to discuss on the nature of the elasticity (due entropic and/or isentropic coupling) [3–6], to identify the mean intrinsic dissipation due to viscosity and/or damage [7–9], to evaluate the strain-induced crystallinity [10,11], and to enrich the modeling of these phenomena [12]. The calorimetric approach is therefore a powerful tool for elastomer mechanics. It should be noted that studies are generally carried out under homogeneous strain fields, typically induced by uniaxial tensile loadings when the temperature field in the measurement zone is assumed to be homogeneous. However, many situations studied in mechanics and mechanical engineering deal with heterogeneous strain fields and should also benefit from such calorimetric approaches. In the case of small deformations, more exactly small displacements of points at the surface observed, measuring thermal fields by infrared (IR) cameras gives access to the temperature evolution at any point of the field and enables us to characterize both temporal and spatial gradients in the thermal response. The heat source fields can be calculated from the temperature variation one, which provides the calorimetric signature of heterogeneities, whatever they are due to the type of loading, specimen geometry or material effects.

* Corresponding author.
E-mail address: jean-benoit.lecam@univ-rennes1.fr (J.-B. Le Cam).

https://doi.org/10.1016/j.polymer.2025.129286
Received 16 June 2025; Received in revised form 21 October 2025; Accepted 1 November 2025
Available online 8 November 2025

Under certain assumptions, the mean intrinsic dissipation field can also be characterized, which is of first importance to enrich and to validate models. For further information, the reader can refer to [13–19]. In the case of large heterogeneous deformations, typically those undergone by elastomers, the points observed with an infrared camera move from one position to another in the successive infrared images. Therefore, only spatial heterogeneities can be discussed at a given time or deformation level, for instance at the maximum opening of a crack [20,21]. The measurement provides information on the temperature distribution at the crack tip, but this distribution is generally affected by conducto-convective effects (the tests are not adiabatic). Therefore, the same mechanical loading conditions possibly lead to different temperature fields, depending on heat diffusion conditions and does not enable us to characterize the thermomechanical couplings, especially the thermoelastic couplings, even less the mean intrinsic dissipation from the measurement. This is the reason why determining the heat source is of a main interest. This requires knowing the position of the points in the infrared (IR) images at any time. Therefore, a full kinematic field measurement must be coupled with the full thermal field measurement. In the case of large deformations undergone by elastomers, Digital Image Correlation (DIC) is probably the most suitable technique to track points at the surface of highly stretched specimens [22,23]. In the case of moderate strain gradients, two studies are reported in the literature. In [24], the authors combined DIC and IR thermography to map displacement, strain, temperature and heat source fields in the case of a stretched 3-branch rubber specimen. The two techniques were coupled, i.e. a common basis was built, by selecting common points in the visible and thermal images. In [25], the common basis was established using a plate with holes beforehand put at the same place as the specimen to be stretched. The authors reconstructed the heat sources. Assuming a behavior model to calculate the heat sources from the strain field, they identified the constitutive parameters at each point independently, meaning that the identification method they developed from the heat source reconstruction does not require knowing the boundary conditions. More recently, Nozaki et al. [26] applied such an approach for investigating the evolution of nonuniform SIC in unfilled NR under heterogeneous deformation achieved with the planar tension of a specimen with a hole. In the case of high strain gradient, typically in the vicinity of a stretched crack tip, only the two studies by Samaca Martinez and coworkers has determined the heat sources field at the crack tip zone in a carbon black filled styrene Butadiene Rubber (SBR) [27] and both in carbon black filled Natural Rubber (NR) and SBR [28]. The authors demonstrated that such a calorimetric approach is promising for characterizing the thermomechanical behaviors of crack tip zones and for highlighting the effects of the Strain-Induced Crystallization (SIC). In all these exploratory studies, the metrology of the coupling technique was not addressed. Therefore, no information is provided on the resolution of the thermal field after coupling, even less on the resolution of the heat source. However, such metrological information is required to go further since heat sources are determined from space and time-based derivatives, and that the mean intrinsic dissipation and crystallinity maps are both obtained by integrating the heat source over time. The present study aims to propose a methodology for determining the optimal conditions for characterizing the heat source field in high temperature and strain gradient zones such as crack tip. The method couples IR thermography and DIC techniques for compensating the point motion in the successive IR images. A full metrological characterization is carried out in order to evaluate the thermal resolution after motion compensation and the heat source resolution.

The paper is organized as follows. Section 2 briefly recalls the theoretical background for reconstructing the heat source fields from temperature field measurements. Section 3 presents the methodology for compensating the movement of points in the IR images. A metrological study circumscribed to the experimental devices used has been carried out in the case of a rigid body motion in order to validate the methodology. The influence of many parameters of different nature has been investigated; parameters used for the DIC, parameters linked to the equipment used (distance of the cameras, the loading rate, the acquisition frequency, the relative spatial resolution of the cameras, etc.). It is presented in Section 4. Then, the methodology has been has applied to the numerical simulation of a homogeneous tensile test of a hyperelastic material in order to investigate what are the best parameters to optimize the heat source resolution and its spatial resolution. The last part of the section aims at defining in which extend the conductive term of the heat diffusion equation can be determined accurately in case of high temperature gradients. This experimental setup and the methodology developed are used in the second part of the present paper in order to map the strain, the heat source and the crystallinity fields at the crack tip of a notched rubber specimen under cyclic loading.

2. Theoretical background for surface calorimetry

Quantitative surface calorimetry (QSC) lies in the determination (the reconstruction) of the heat source from temperature measurements at the surface of a material and the heat diffusion equation [29]. If the thermal measurement provides bidimensional fields, typically when using an IR camera at the flat surface of a specimen, the tridimensional formulation of the heat diffusion equation has to be simplified accordingly [2]. This is all the more justified if the heat sources are homogeneous or if heat conduction is negligible.

2.1. Tridimensional heat diffusion equation

In the case where the constitutive state equations are derived from the Helmholtz free energy function and that heat conduction follows Fourier's law, the lagrangian formulation of the local heat diffusion equation writes as follows:

$$\rho_0 C\dot{T} + \mathrm{Div}\mathrm{Q} - R = \hat{S} \tag{1}$$

with ρ_0 the initial mass density, C the heat capacity, T the absolute temperature, Q the heat flux per unit reference area and R the external radiations. Note that $\mathrm{Q} = -det(\mathbf{F})\ \mathbf{F}^{-1}\mathbf{K_0}\mathbf{F}^{-\mathrm{T}}\mathrm{Grad}\,T$, where $\mathbf{K_0}$ is the thermal conductivity tensor. The superposed dot stands for the material time derivative.

2.2. Simplification of the heat diffusion equation

The temperature fields provided by IR thermography are bidimensional. Reconstructing the heat source field from them requires therefore the formulation of a two-dimensional version of the heat diffusion equation. To this end, several assumptions are successively made. Here, the heat conduction is considered as isotropic (the thermal conductivity coefficient is denoted k_0 in the following)[1] and the temperature as constant over the specimen thickness. Moreover, the material is considered as incompressible. If the specimen is relatively thin, Eq. (1) can be integrated over the thickness,[2] which leads to the following two-dimensional formulation of the heat diffusion equation

$$\rho_0 C\left(\dot{T} + \frac{T - T_{amb}}{\tau_{2D}}\right) - \mathrm{Div}_{2\mathrm{D}}(k_0\mathbf{C}^{-1}\mathrm{Grad}_{2\mathrm{D}}\,T) - R = \hat{S}, \tag{2}$$

[1] It should be noted that this assumption can be strong in the case of very large deformations undergone by elastomers. Nevertheless, the conduction term is generally neglected in most calorimetric approaches applied to stretched elastomers. Therefore, even though our methodology can be improved, it allows us to go further in the determination of heat sources under large strains by integrating the calculation of a conduction term.

[2] The relevancy of this assumption (homogeneous temperature in the thickness direction) for a given situation can be evaluated by calculating the Biot number B_i [30].

where T_{amb} is the ambient temperature. $\mathbf{C} = \mathbf{F}^{\mathbf{T}}\mathbf{F}$ is the right Cauchy–Green tensor. τ_{2D} is a time characterizing the heat exchanges along the thickness direction by convection with the air at the specimen surface. If the external radiations R are constant during the deformation process, they can be removed from the heat diffusion equation by using the temperature variation $\theta(X,Y,t) = T(X,Y,t) - T_{ref}(X,Y)$ instead of the temperature itself. It should be noted that T_{ref} is the ambient temperature if it remains constant over the test. In this case, Eq. (2) writes:

$$\rho_0 C\left(\dot{\theta} + \frac{\theta}{\tau_{2D}}\right) - \mathrm{Div}_{2D}(k_0 \mathbf{C}^{-1}\mathrm{Grad}_{2D}\,\theta) = \hat{S}. \tag{3}$$

For the sake of simplicity, τ_{2D} is denoted τ in the following. τ can be characterized from a natural return to room temperature after a heating (or a cooling) for each testing configuration (machine used, environment, etc.). Indeed, in this case $\theta = \theta_0 e^{\frac{-(t-t_0)}{\tau}}$. Either τ is determined at different increasing stretches as done in [5], or it can be obtained in the undeformed state and corrected according to its dependency on the stretch and the multiaxiality state as follows, assuming the material to be incompressible [25]:

$$\tau = \tau(\lambda_I, B) = \tau_0 \lambda_I^{-B-1}, \tag{4}$$

where $B = \frac{ln\lambda_{II}}{ln\lambda_I}$ denotes the biaxiality ratio [31,32], defined as the ratio of the logarithm of the minimum by the maximum in-plane principal stretches, respectively.

Under equi-biaxial tension, pure shear, and uniaxial tension, B is equal to 1, 0 and −0.5, respectively. Here, τ_0 is characterized from the return to the ambient temperature of a heated undeformed specimen. The evolution of τ with the stretch is then given by Eq. (4). Note that τ is determined without any displacement of the specimen in air. In the present paper, the specimens are stretched symmetrically in order to limit additional heat convection due to displacement of the measurement surface in air and to meet the same conditions as those for determining τ. Finally, it should be noted that Eq. (3) is formulated in the case where the ambient temperature T_{amb} is constant during the test. In case where changes in ambient temperature occur, the term $\frac{\theta}{\tau}$ has to be corrected accordingly and replaced by $\frac{T-T_{amb}}{\tau}$.

When the material points move from one pixel to another in the IR images, the bi-dimensional formulation of the heat diffusion equation does not apply directly and material points have to be tracked in the IR images. For that purpose, kinematic field measurements must be performed and coupled to the thermal field measurements. This is explained in the next section.

3. Coupling the infrared and visible images

Applying Eq. (3) requires knowledge of the displacement and the temperature variation of any material point at any time. The large deformations undergone by elastomeric materials induce large displacements of the material points. Therefore, measurement of the kinematic field has to be carried out during the test in order to track the material points in the infrared images. Fig. 1 gives a schematic view of the experimental setup used. In this configuration, the charge-coupled device (CCD) and IR cameras are placed on both sides of the specimen and their detector centers and the zone of interest center are aligned, but this is not mandatory. It should be noted that in the case of small deformations (inferior to 10%), the measurements (kinematic and thermal) have already been done on the same specimen's side [33,34] with a dichroic mirror. The authors investigated the heterogeneities in strain and temperature fields at the microstructural level of polycrystalline metals. Moreover, in the study due to [35], only one IR camera was employed and a limited number of reflective points at the surface of a stretched filled notched NR specimen were tracked in IR images during the test, which leads to a very low resolution relatively to the strain gradient expected at the crack tip. Up to now, measuring the two full fields on the same side has not been yet carried out in the case of large deformations. This is currently investigated in our team for large thickness specimens, for which the assumption of homogeneous temperature field in the thickness of heterogeneous materials appears as too strong (kinematic and thermal fields different from one side to another). A uniform cold lighting at the specimen surface is ensured by a home-made LED lamp on the CCD camera side. A glass window of emissivity equal to 0.84 is put between the CCD camera and the specimen and is oriented at 45° in order to limit the reflexion effect, as a black body is placed at 90° of the IR camera axis. Therefore, the radiations emitted and received by the camera are due to the specimen itself. Furthermore, the whole device is protected from external radiations by using a box made of high emissivity materials that is not represented in the figure. Distances between the visible camera and the specimen as well as the distance between the IR camera and the specimen are respectively denoted L_{VIS} and L_{IR} in the rest of the paper.

The aim of the coupling method is to be able to transfer information from the visible images to the IR ones by using a common basis. For that purpose, a spatial calibration procedure is done to couple the two cameras before performing the test. The calibration is performed by using a calibration pattern, which is composed of two sets of four holes that form a large rectangle and a small square patterns, as shown in Fig. 2. Here, the large rectangle (ABCD) has been chosen. The size of the pattern chosen depends on the area of the zone to be observed. The calibration pattern is placed at the same location as the specimen is during the test, so that the four points A, B, C and D appear in both the visible and the IR images. Their position in the visible and the IR images is determined as follows using a mark tracking algorithm:

- the area that contains each marker (point) is selected by hand, as shown in Fig. 3(a),
- for each area (for instance the one in Fig. 3(b)), a threshold is defined, i.e. each pixel value is compared with a reference one. Each pixel under this reference value is set to 0 (full black pixel) and each pixel over it is set to 255 (full white pixel). Fig. 3(c) presents the resulting thresholding for a single marker area,
- the barycenter of zones of either black or white pixels is calculated (see Fig. 3(d)). This operation is made for the four markers. At the end of the mark tracking algorithm, the position of the four markers in both CCD and IR images is known and a common basis can be defined to transfer the coordinates of the CCD and IR points.

For both images, an affine transformation (translation and rotation) and a scaling operation (converting pixel to millimeter) are performed considering point C (see Fig. 3) as the origin of the common coordinate system. As an example, for the CCD camera this operation is performed using the following formulation:

$$x_{translation} = \left(X_{camera} - X_{C_{camera}}\right)\frac{L_X}{I_{opt}} \tag{5}$$

with

$$I_{opt} = cos(\alpha) * (\Delta X) - sin(\alpha) * (\Delta Y) \tag{6}$$

and

$$y_{translation} = \left(Y_{camera} - Y_{C_{camera}}\right)\frac{L_Y}{J_{opt}} \tag{7}$$

with

$$J_{opt} = sin(\alpha) * (\Delta X) + cos(\alpha) * (\Delta Y) \tag{8}$$

with x and y the position in the translated coordinate system (in mm), X_{camera} and Y_{camera} the position of the pixel in the camera coordinate system (in pixels), $X_{C_{camera}}$ and $Y_{C_{camera}}$ the position of point C in the camera coordinate system (in pixel), α the angular deviation between the two coordinate systems, ΔX and ΔY are respectively the horizontal and vertical distances between two measured markers in the image (in

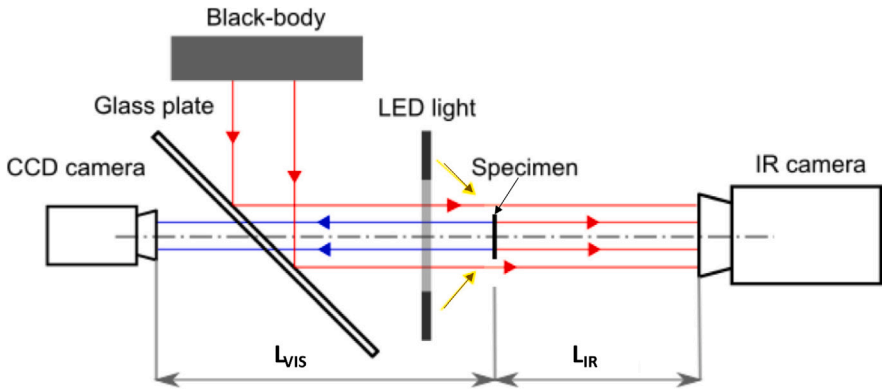

Fig. 1. Schematic view of the experimental setup. The two cameras are located on both sides of the specimen. A glass plate is positioned between the CCD camera and the specimen in order to limit the external radiations from the CCD camera side. A black-body (emissivity close to 1) is placed perpendicularly to the cameras axes in order to limit reflexion effects at the glass plate surface. The red lines stand for the very small external infrared radiations reflected by the glass plate and for the particles emitted by the specimen. The blue lines illustrate the rays of light parallel to the optical axis between the CCD camera and the specimen surface.

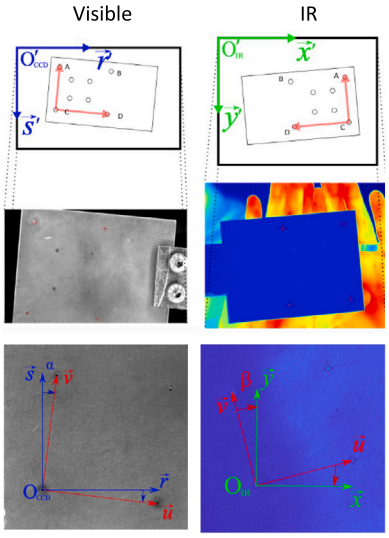

Fig. 2. Calibration pattern and bases necessary to couple visible and IR images. The angle shift is voluntary in order to evaluate the angular correction accuracy.

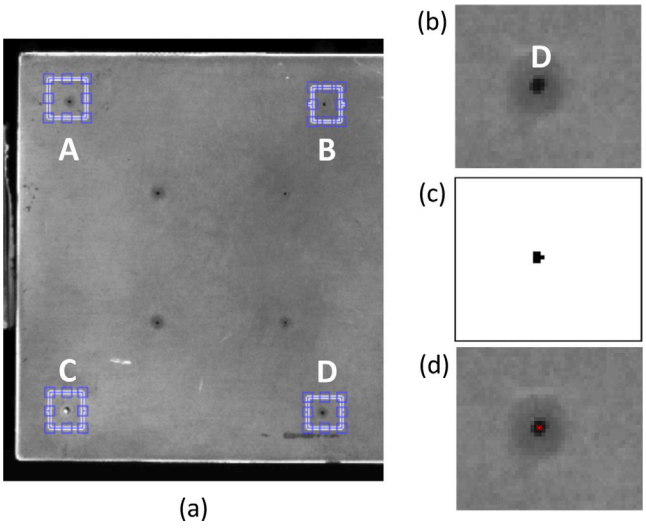

Fig. 3. Illustration of the mark detection algorithm used for determining the coordinates of points A, B, C and D. (a) Selection of the four points A, B, C and D (b) Zoom in the region of point D (c) Thresholding step (d) identifying the barycenter of the zone corresponding to point D.

pixel) and L_X and L_Y are the horizontal and vertical distances between two markers on the calibration pattern (in mm). This procedure is also carried out for the IR images. In Fig. 2, $< O'_{CCD}/\vec{r},\vec{s}' >$ and $< O'_{IR}/\vec{x}',\vec{y}' >$ are coordinate systems that is used by Matlab software for reading CDD and IR mages respectively.

Once the infrared and visible images are coupled, the temperature monitoring of each material point can be obtained if their displacement is known. In the present case, the kinematic field is obtained by the DIC technique, which is well adapted and generally used in the case of large deformations. The principle of the method consists in comparing two digital images of a specimen surface with a random gray pattern (or speckle). This pattern can be natural if the gray level distribution meets the DIC requirements, for instance with the roughness of the material [36], or artificial, typically by spraying paint at the specimen surface. Matt paint must be used to avoid any reflection. The software used for the correlation process was 7D [37]. From the displacements, the principal stretches (λ_I λ_{II}) and the biaxiality ratio (B) are determined in order to calculate τ_{2D} in Eq. (2). For that purpose, square elements are created, each corner of a square element corresponding to a grid node where the displacement has been determined. Within a square element i, the horizontal and vertical displacements, ${}^iU$ and ${}^iV$ respectively, are assumed to be bilinear of the position:

$$\begin{cases} {}^iU(X,Y) = a + bX + cY + dXY \\ {}^iV(X,Y) = e + fX + gY + hXY \end{cases} \tag{9}$$

with a, b, c, d, e, f, g and h eight parameters that can be identified from displacement measurement of the four corner of the square element. The calculation is carried out by considering the square element center to be the origin of the coordinate system. Finally, the deformation gradient tensor $\mathbf{F}$ at the square element center is obtained by using Eq. (10):

$$\mathbf{F} = \begin{pmatrix} \frac{\partial x}{\partial X} & \frac{\partial x}{\partial Y} \\ \frac{\partial y}{\partial X} & \frac{\partial y}{\partial Y} \end{pmatrix} = \begin{pmatrix} \frac{\partial X + {}^iU}{\partial X} & \frac{\partial X + {}^iU}{\partial Y} \\ \frac{\partial Y + {}^iV}{\partial X} & \frac{\partial Y + {}^iV}{\partial Y} \end{pmatrix} = \begin{pmatrix} 1+b & c \\ f & 1+g \end{pmatrix} \tag{10}$$

From the gradient deformation tensor obtained, the principal stretches are easily deduced. First, the left Cauchy–Green tensor $\mathbf{B} = \mathbf{F}\mathbf{F}^T$ is calculated and diagonalized, which gives:

$$\mathbf{B} = \begin{pmatrix} \lambda_I^2 & 0 \\ 0 & \lambda_{II}^2 \end{pmatrix} \tag{11}$$

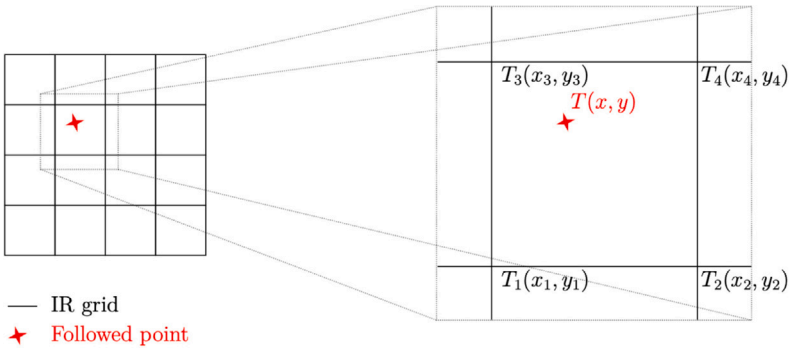

Fig. 4. Illustration of the bilinear interpolation of the temperature field at a tracked point of the visible image. The tracked point is a node of the correlation grid.

with $\lambda_I \geq \lambda_{II}$, where λ_I and λ_{II} are the maximal and minimal in-plane principal stretches, respectively.

To summarize, once the cameras are coupled and the kinematic fields obtained, the position of each point can be theoretically tracked in the IR images. Nevertheless, it should be noted that:

- the spatial resolution of the two cameras is different,
- the DIC does not provide an integer number of pixels for the displacement.

Therefore, the tracked points in the visible images will not move from a pixel to another in the infrared images, but in between. This is why the temperature field is first interpolated by a bilinear function, using the neighboring IR pixels, as illustrated in Fig. 4. The temperature at a tracked point is given by:

$$T(x, y) = ax + by + cxy + d \tag{12}$$

with T the temperature of the material point tracked, which has a position (x, y), and a, b, c and d four parameters that can be found using the four neighboring IR pixels whose temperature values are T_1, T_2, T_3 and T_4 and positions are (x_1, y_1), (x_2, y_2), (x_3, y_3) and (x_4, y_4), respectively.

4. Metrological characterization of the method

In this section, the motion compensation technique and more precisely the sensibility of the thermal resolution to the different parameters is evaluated, in the range of variation enabled by both the experimental setup and the data processing method used. This has been carried out from the rigid body displacement of a thermal pattern. This study is presented in Section 4.1. Then, a numerical study described in Section 4.2 is dedicated to the determination of the heat source during the stretching of a rubber specimen. This study enables us to estimate the resolution of the heat source, since the problem considered has an analytical solution. Finally, even though the heat diffusion is small in rubbery material, i.e. the laplacian term in Eq. (3) does not contribute significantly to the heat source, a numerical study is finally proposed in Section 4.3 in order to discuss on the strategy for calculating the laplacian term for two different temperature gradient levels.

4.1. Validation of the motion compensation technique and effect of the experimental and data processing parameters on the thermal resolution

In order to validate the technique, it has been applied to a corrugated cardboard glued on a metallic plate painted in black color moved horizontally (see Fig. 5(a)). Here, the temperature of the cardboard is homogeneous, but the apparent emissivity and therefore the temperature field measured by the IR camera is heterogeneous due to the cardboard waves (see Fig. 5(b)). Indeed, the surface is not perpendicular to the IR detector matrix at any point, and surfaces

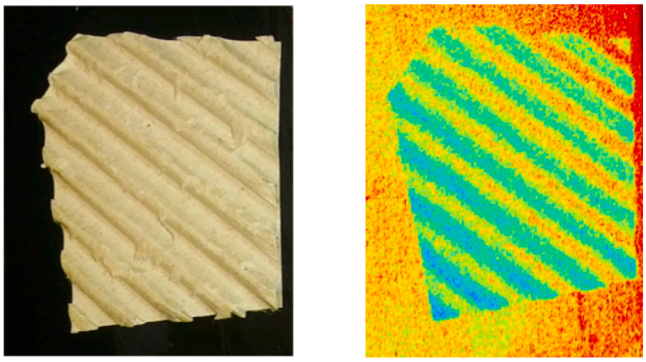

Fig. 5. Visible (a) and IR (b) images of the corrugated cardboard glued on a metallic plate painted in black color.

closer to the IR detector matrix appear periodically colder. It should be noted that temperature variations due to waves are one order of magnitude superior to the thermal resolution of the camera. Here, the Noise-Equivalent Temperature Difference (NETD) is 20 mK in the temperature range between 5 and 40 °C. Thus, if the motion of points is not accurately compensated in the IR images, the standard deviation of the temperature variation at any point should significantly increase. In other words, the technique can be validated if the wave-like pattern is still observed from one IR image to another and if the mean standard deviation is close to the thermal resolution of the camera.

4.1.1. Kinematic field measurement

Images of the specimen surface at increasing stretches were stored with a IDS UI-3160CP Rev. 2 camera equipped with a 55 mm telecentric objective. The objective is C-mount partially telecentric, with constant magnification over a range of working distances ±12.5 mm of object movement before 1% error image scale occurs. The CCD of the camera has 1920 × 1200 joined pixels. A uniform cold lighting at the specimen surface is ensured by a home-made cold LED lamp. The camera was fixed on a multidirectional adjustable support. The software used for the correlation process was 7D [37]. Three main parameters could have an influence on the thermal resolution and will be considered in the following; the subset size, the step size and the gray level interpolation function (the interpolant) (see [38] for further details on the terminology).

4.1.2. Thermal field measurement

Temperature measurement was performed with a cooled high-resolution FLIR X6540sc infrared camera equipped with a focal plane array of 640 × 512 pixels and detectors operating in wavelengths

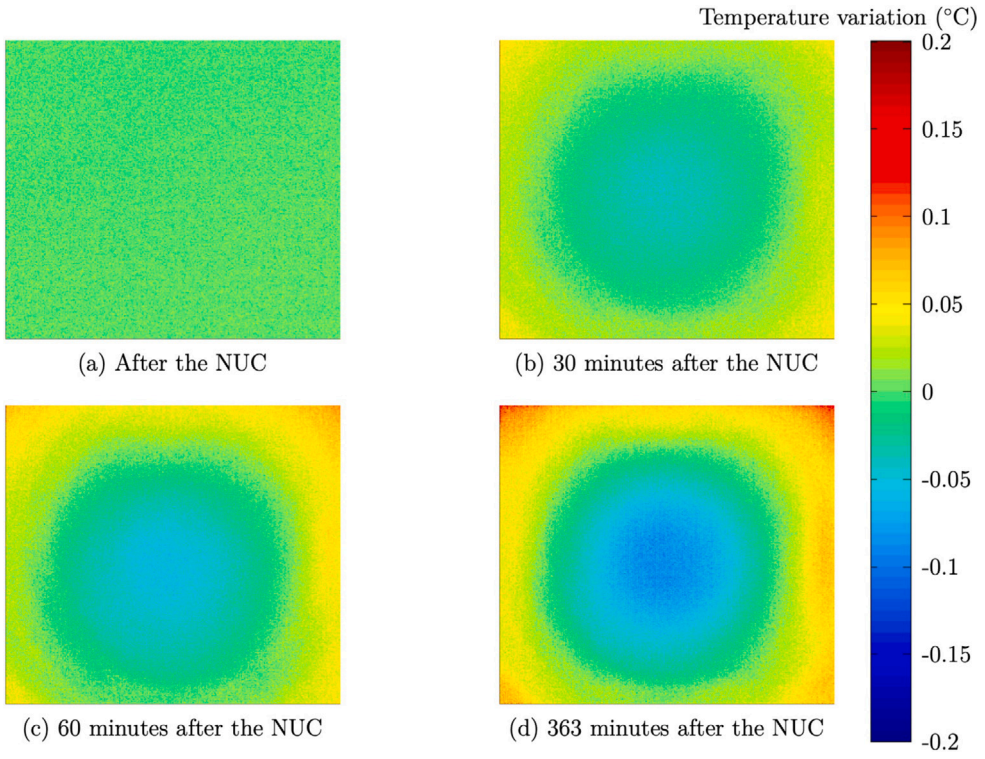

Fig. 6. IR images of a black body surface at the same temperature at different times after the NUC procedure.

between 1.5 and 5.1 μm. The integration time was equal to 2.623 ms. The image acquisition was triggered at the same frequency as the CCD camera. The calibration of camera detectors was performed with a DCN1000N12 HGH Infrared Systems black body using a one-point non-uniformity correction (NUC) procedure at this acquisition frequency. The infrared camera was switched on 60 min before the test in order to stabilize its internal temperature. In the case where the correction of the temperature measurement according to the IR detector temperature has been shunted, it should be noted that temperature measurements can be strongly affected by the occurrence of a halo effect even though the NUC procedure has been performed. This shunt is made to avoid automatic temperature correction, which would lead to a jump in temperature evolution. This halo can be illustrated by Fig. 6 that gives IR images of a black body stored at different times after the NUC procedure. This figure clearly shows that in spite of the NUC, the halo pattern reappears with time.

Fig. 7 shows the time evolution of the amplitude of temperature values over the whole field (max(T) - min(T), at the top). A 3D map of the temperature fields at different times is provided at the bottom. This figure clearly shows that the halo pattern intensifies strongly the first hour. Therefore, it can strongly affect the thermal resolution of the motion compensation technique, as the points of the surface observed move through the halo. From 1 h on, the maximum temperature amplitudes between two points in the thermal field vary little over time. More specifically, for a 1 min measurement duration, i.e. the case in the present study, the difference is 0.00035 K, which is a variation two orders of magnitude lower than the camera's NETD. Therefore, no real-time correction is needed. This is why we turn on the camera two hours before performing the NUC and start the measurement, which lasts about one minute. It should be noted that if the measurement is longer, it is recommended to activate an automatic real-time correction and to switch on the camera several hours before doing the NUC and starting the measurement.

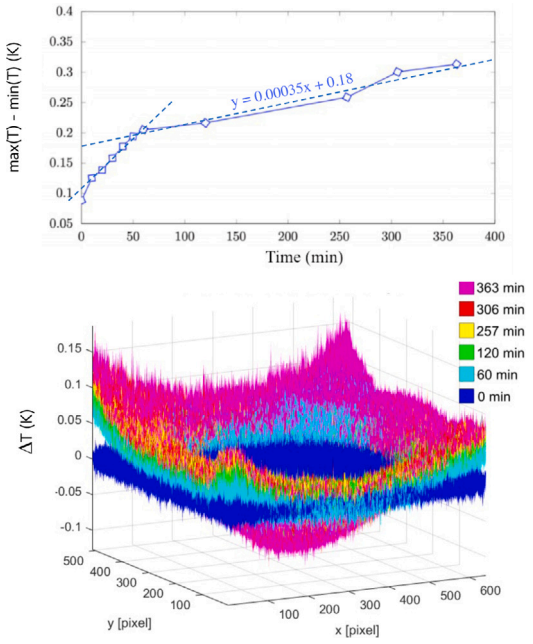

Fig. 7. Evolution of the amplitude of the temperature value (max(T) - min(T)) in the field (top). Evolution of the halo pattern (bottom).

A noteworthy problem is due to the infrared environment of the IR camera, typically the reflexion of the IR detector matrix in the visible camera lens. This issue is solved by positioning a glass plate of thermal emissivity equal to 0.84 between the LED light and the specimen. A

Table 1
The 11 configurations considered for the experimental parameters.

Configuration number	frequency (frame/s)	loading rate (mm/min)	L_{VIS} (mm)	L_{IR} (mm)	R_{VIS} (mm/px)	R_{IR} (mm/px)	$<\sigma>$ with filtering (K)	$<\sigma>$ without filtering (K)
#1	5	300	70	50	0.059	0.17	0.0179	0.0199
#2	10	75	70	50	0.059	0.17	0.0164	0.0212
#3	10	150	70	50	0.059	0.17	0.0192	0.0242
#4	10	225	70	50	0.059	0.17	0.0147	0.0198
#5	10	300	70	50	0.059	0.17	0.0152	0.0212
#6	10	300	140	50	0.118	0.17	0.0192	0.0192
#7	10	300	140	110	0.118	0.35	0.016	0.0206
#8	10	300	140	176	0.118	0.54	0.0143	0.0203
#9	10	300	190	50	0.165	0.17	0.0194	0.0225
#10	15	300	70	50	0.059	0.17	0.0158	0.021
#11	20	300	70	50	0.059	0.17	0.0151	0.02

black body is placed at an angle of 45° to limit the incident radiation on the glass plate (see Fig. 1).

4.1.3. Parameters considered for the metrological characterization

The experimental parameters whose influence on the thermal resolution is investigated are the loading rate, the acquisition frequency, the distance between the IR detector (L_{IR}) and the specimen as well as the distance between the CCD detector and the specimen (L_{VIS}). The influence of the step size, the subset size and the interpolation function was also investigated for the DIC technique, as well as the temporal filtering of the temperature variations. The effect of the different parameters is addressed with several configurations. The values of the different parameters for each configuration are summarized in Table 1. They have been chosen accordingly to the features and limitations of the experimental setup used. In this table, the spatial resolution of the visible (R_{VIS}) and the IR (R_{IR}) images are given for each configuration.

These configurations were tested without and with an averaging temporal filter of size 3, which is the minimum size, applied to process the temperature variation. A grid step of 10 pixels and a subset size of 10 pixels were used for the DIC. Here, no spatial filtering is applied on the visible and infrared images. Note that the interpolation of the temperature at the position of the correlation grip nodes indirectly slightly filters the temporal field. Nevertheless, the effect is very small as the IR image resolution is of the same order of magnitude as the visible image one. It should be noted that when the distance between the specimen and the cameras is changed, the size of the windows where the specimen is moved changes. The displacement is adjusted accordingly. This means that even though both the acquisition frequency and the distance of the cameras are changed in order to fully meet the experimental conditions, it changes the number of temperature values for calculating the standard deviation σ and the mean standard deviation $<\sigma>$. The effect of high loading rates can be limited by increasing the frequency and reducing the integration time, but this requires changing the type of lighting. The results reported in this study is therefore relative to LED lamp used. The maximum loading rate and maximum frequency applied with this configuration is 300 mm/min and 20 Hz, respectively. Parameters due to the image processing have also been investigated by considering configuration #5. It is chosen as it provides an intermediary thermal resolution (presented in the results section). The type of interpolation function (bilinear or bicubic), the grid step and the subset size. They are reported in Table 2.

4.1.4. Results obtained with the motion point compensation method

Fig. 8 illustrates the compensation of the point motion in the IR field. This figure shows IR images of the cardboard plotted in the visible images once the calibration procedure is done. The scale is the same for the three temperature fields considered. From a qualitative point of view, it is shown that the pattern is well tracked. In order to evaluate the thermal resolution, the standard deviation of the temperature variation signal is calculated at any point of the field during a return trip in translation. The mean of the standard deviation field is then calculated for each configuration and the value is reported in Tables 1 and 2. Since no temperature variation should occur during the translation, the performance of the method will be evaluated by measuring the standard deviation of the temperature of each material point and compared with the Noise Equivalent Temperature Deviation (NETD of 20 mK) of the IR camera.

Table 2
The 19 configurations considered for investigating the effect of the DIC parameters.

Configuration number	grid step grid step	subset size subset size	interpolation function	Mean standard deviation
#12	10	6	Bicubic	0.0148
#13	10	8	Bicubic	0.0148
#14	6	10	Bicubic	0.0149
#15	8	10	Bicubic	0.0149
#16	10	10	Bicubic	0.0149
#17	12	10	Bicubic	0.0149
#18	10	12	Bicubic	0.0148
#19	10	16	Bicubic	0.0149
#20	10	20	Bicubic	0.0149
#21	10	4	Bilinear	0.0148
#22	10	6	Bilinear	0.0148
#23	10	8	Bilinear	0.0149
#24	6	10	Bilinear	0.0149
#25	8	10	Bilinear	0.0149
#26	10	10	Bilinear	0.0149
#27	12	10	Bilinear	0.0149
#28	10	12	Bilinear	0.0149
#39	10	16	Bilinear	0.0149
#30	10	20	Bilinear	0.0149

The first parameter studied is the image acquisition frequency. The corresponding configuration numbers are 1, 5, 10 and 11 (frequencies in blue color in Table 1). The loading rate and the distance between the cameras and the specimen were kept constant. Fig. 9(a–d) show the cartography of the standard deviation of the temperature variation. It is close to the NETD of the IR camera, the maximum value being equal to 29 mK. As seen on these maps, a pattern that corresponds to the pattern of the cardboard is observed. It is recalled that the apparent temperature variation due to the cardboard waves of one order of magnitude higher that the camera's NETD. The mean standard deviation for each frequency is given in Fig. 9(e). The acquisition frequency seems to have only a small influence on the performance. In this figure, it is shown that a minimum centered temporal filtering size of 3 decreases the thermal resolution below the camera's NETD.

The second parameter studied is the loading rate, the other parameters being kept constant. The corresponding configuration numbers are 2, 3, 4, and 5 (loading rates in green color in Table 1). Fig. 10(a–d) show the cartography of the standard deviation of the temperature variation. Fig. 10(e) gives the mean standard deviation versus the loading rate. In the loading rate range studied, the performance of the motion compensation technique in terms of the mean standard deviation of the temperature variation does not evolve significantly. It should be noted that with a higher loading rate, visible images become blurred, which impacts the accuracy of the DIC technique, and by extension of the motion compensation method.

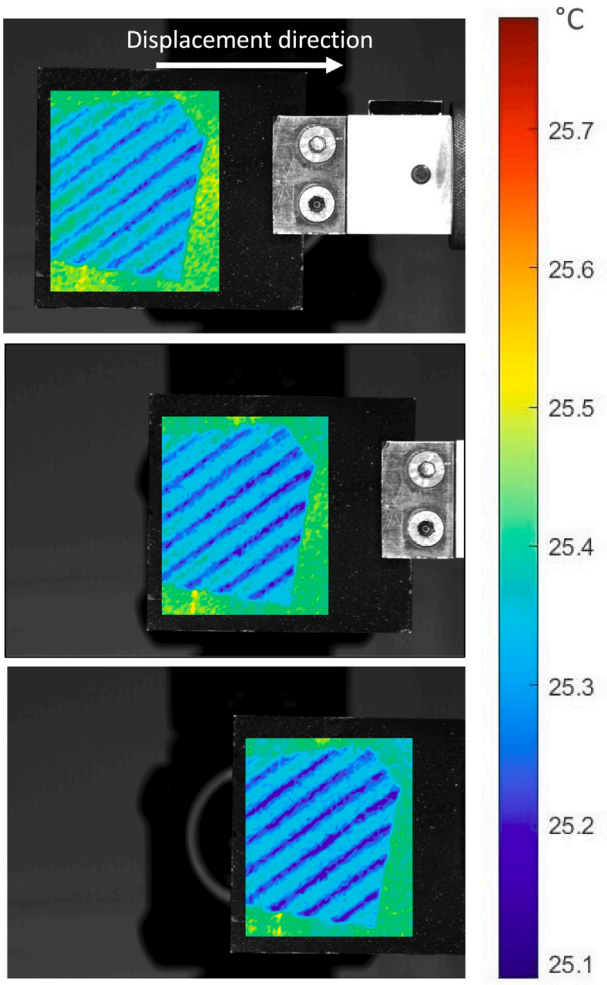

Fig. 8. IR images of the cardboard plotted at different positions in the visible images.

The third parameter studied is the distance between the specimen and the visible camera (configurations #5, #6, and #9, (L_{VIS} in red color in Table 1)). Fig. 11(a–c) show the cartography of the standard deviation of the temperature variation. As for the previous results obtained, the temperature pattern is visible except for the lowest distance. The thermal resolution is higher for the lowest distances. This could be easily explained by the fact that with a higher distance, the spatial resolution of the camera increases, i.e. each pixel corresponds to a larger area of the specimen. In that case, a same error in the DIC technique in term of pixel leads to a higher error of the displacement on the specimen, and in the case of heterogeneous temperature field, an higher error on the temperature tracked.

Fig. 11(d) gives the mean standard deviation for each configuration.

The last parameter studied is the distance between the specimen and the IR camera (configurations #6, #7, and #8, (L_{IR} in magenta color in Table 1)). Fig. 12(a–c) show the cartography of the standard deviation of the temperature variation. As for the previous results obtained, the pattern is visible. Fig. 12(d) represents the mean standard deviation for each test. In the distance range studied, the performance of the motion compensation technique does not evolve strongly. However, with a higher distance, the spatial resolution of the IR images increases, which decreases the precision, especially for high temperature gradient. Finally, the parameters relative to the DIC have been investigated and the results in terms of the mean standard deviation of the temperature variation is reported in Table 2. For that purpose, configuration #5 is considered. This configuration is for the highest loading rate, intermediary frequency and distance of the cameras. It is the closer from experimental conditions required with the rubber specimens used with this experimental setup. The grid step, the subset size and the interpolation function are changed. The results obtained shows that these parameters have no significant effect on the thermal resolution after motion compensation, which is logical as the Zones of Interest (ZOIs) tracked do not deform.

To conclude, the influence of different experimental parameters on the motion compensation of the material points in the infrared images has been investigated. For all the configurations investigated, which are defined with respect to the features of our experimental setup, the temperature standard deviation found is close to the NETD of the IR camera, which validates the motion compensation technique. The most influential is the distance between the visible camera and the specimen, since a same displacement error (in pixel) leads to a higher error of the displacement (in mm) when it is increased, and in the case of heterogeneous temperature field, this leads to a higher error in the tracking of material points in the IR images and therefore a higher temperature error. It was also shown that filtering temporally the temperature variations, even with the lowest filter size, decreases the thermal resolution below the one of the IR camera. The results of this first metrological study, showing that the motion compensation technique does not alter the thermal resolution is of first importance as the thermal field is then derived to apply the heat diffusion equation for calculating the heat source. The next metrological study aims at characterizing the heat source resolution and therefore must be carried out in the case of a large deformation process.

4.2. Numerical study of the heat source resolution

The previous test, corresponding to a rigid-body motion, allowed us to validate the motion compensation technique using the spatial calibration of the two cameras. It also shows that the temperature noise obtained after the motion compensation technique is mostly due to the thermal sensitivity of the IR camera. In other terms the numerical processing for the motion compensation does not alter the thermal resolution. To estimate errors on both deformation and heat source fields, a procedure has to be defined. It consists in simulating a uniaxial tensile test. The motion compensation technique is applied to the set of images obtained from numerical simulations in order to deform accordingly the speckle. It is precisely described in the following.

4.2.1. Generation of simulated kinematic and thermal fields

In order to evaluate the errors on the heat sources, the heat sources are first computed numerically. A mechanical test consisting in stretching homogeneously a rectangular specimen is simulated by the finite element method using the ABAQUS software. The specimen is 123.54 mm in length, 29.82 mm in width and 2 mm in thickness. Opposite vertical displacements of 70 mm are prescribed on the upper and lower grips at a loading rate of 150 mm/min. The mechanical behavior of the specimen, i.e., the strain–stress relationship, is predicted with a Neo-Hookean model. This model has been chosen as its constitutive parameter directly depends on the temperature (see Eq. (2.7), page 765 in [39]), which provides a simple analytic expression of the corresponding heat source induced by the deformation under uniaxial tension (see Eq. (26) in [40]). This model assumes that the elasticity of the material is purely entropic, with no viscosity or crystallization. This is typically the case of the unfilled nitrile rubber used in [25] and this why we used the value of the constitutive parameter the authors found in the case of uniaxial tension (0.24 MPa, issued from Figure 13 in [25]). It should be noted that the sole purpose of this calculation is to evaluate the heat source resolution. The calorimetric approach, on the other hand, is applicable to all types of elastomer, regardless of whether they are viscoelastic or crystallize under stretch.

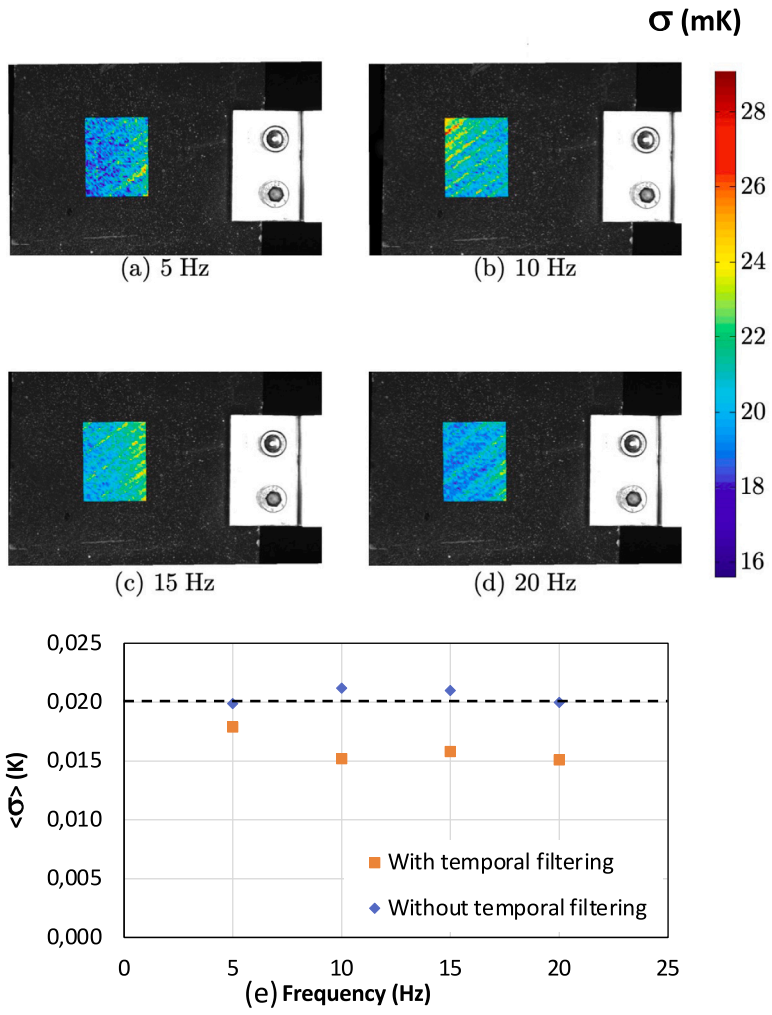

Fig. 9. Cartography of the standard deviation of the temperature variation for different acquisition frequencies ((a) to (d)). Temperature variation is not filtered, neither spatially nor temporally (e) Mean standard deviation of the temperature variation versus the acquisition frequency, with and without temporal filtering (centered filter of size equal to 3).

Visible images are then created by deforming a speckle image by using the displacement field predicted numerically. The spatial resolution is chosen here equal to 0.15 mm/px, the acquisition frequency is chosen equal to 5 Hz. Fig. 13 gives the image of the speckle in the underformed and maximum deformed states.

In order to generate the corresponding IR images, the heat diffusion equation is applied. The initial temperature is supposed to be homogeneous, and equal to 20 °C. The thermal diffusion within the material is neglected, the heat equation can be therefore simplified to its "0D" formulation:

$$S = \rho_0 C \left(\dot{\theta} + \frac{\theta}{\tau} \right) \tag{13}$$

The mass density and the heat capacity are supposed to be constant during the whole test, however the time τ depends on the strain state. For an uniaxial tensile test, assuming that the material is incompressible, τ can be obtained using the following formulation:

$$\tau = \frac{\tau_0}{\sqrt{\lambda}} \tag{14}$$

Neo-Hookean model is used to determine the heat source produced by the material (more details are provided in [25,40]), and is expressed as followed for uniaxial tension:

$$S = 2C_{nh} \left(\lambda - \lambda^{-2} \right) \frac{d\lambda}{dt} \tag{15}$$

After determining the time evolution of the specimen's temperature during the simulated test, IR images are created, by applying a constant temperature equal to 18 °C to each pixel outside the specimen, and the calculated temperature to each pixel inside the specimen. These IR images are computed at the same times as for visible images, at an acquisition frequency of 5 Hz, for a spatial resolution of 0.5 mm/px. In order to better meet experimental IR images obtained with an infrared camera, a thermal noise is added to the images. For this purpose, the thermal noise is characterized for the IR camera. Fig. 14 represents the power density and probability density of the measured thermal noise, and shows that the noise can be modeled using a white noise with a standard deviation of 20 mK, i.e. the noise added has a mean value equal to 0 K and a standard deviation equal to 20 mK.

Fig. 15 represented IR images obtained using this method for the undeformed and maximum deformation states.

4.2.2. Kinematic field determination

First, a metrological study on the kinematic field is performed. For that purpose, DIC is performed, using the software 7D, on numerical

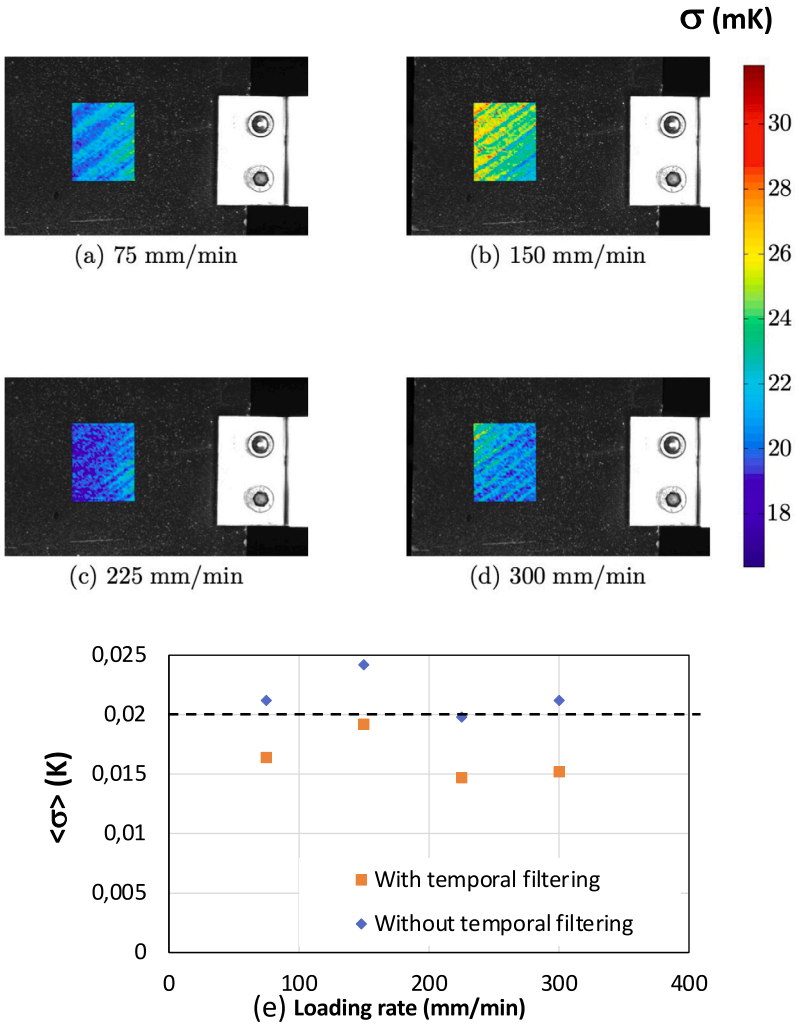

Fig. 10. Cartography of the standard deviation of the temperature variation obtained for several loading rate ((a) to (d)) (e) Mean standard deviation of the temperature variation versus the loading rate, with and without temporal filtering (centered filter of size equal to 3).

visible images. For this study, the grid step is set to 10 pixels and the subset size ranges between 4 and 20 pixels.

Fig. 16(a) presents the maximal principal stretch at a single point measured using this method for several ZOI sizes. Fig. 16(b) shows that the relative error is low, 1.8% maximum. From a ZOI (subset) size of 10 pixels on, the relative error on the maximum principal stretch is inferior to 0.58%.

4.2.3. Resolution of the heat source

Using the spatial calibration of the two cameras, the motion compensation technique is performed to measure the temperature at the different points where the kinematic field has been measured. For this study, the ZOI size is fixed to 10 pixels. Then, the heat equation is used to obtain the heat produced by the material during the test. The heat source is measured for raw temperatures and temperature filtered with different filter sizes. In this study, a mean filter is used, and different sizes of filter have been applied to study the influence of the filter on the heat source measured. Fig. 17 presents the heat source measured at a single point for the different filter sizes. The temperature variations are derived with a centered finite difference.

Fig. 18 presents the absolute error for all the filters (Fig. 18(a)) and for a filter size of 15 and 20 (Fig. 18(b)). These figures clearly show that from a temporal filter of size 15 on, the thermal noise from IR images is reduced, so that the maximum absolute error is about 5 10^3. This is one to two orders of magnitude less than the heat source resolution necessary to investigate the thermomechanical response of elastomers (see for instance [5,25,41]).

It should be noted that this filter size is significant as the acquisition frequency is 5 Hz. Obviously, in the case of high temporal temperature gradients (within 1 s typically), the acquisition frequency has to be adjusted according to both the thermal temporal gradient and the temporal filter size. If it is not possible, a more suitable temporal filter has to be used, typically a Savitzky–Golay finite impulse response (FIR) smoothing filter [42] (see Part II).

4.3. Numerical study of the heat diffusion term

The previous metrological study has investigated the effect of the motion compensation method and the kinematic field measurement on the heat source without heat conduction as the strain and the thermal field were homogeneous. In order to investigate the calculation of the heat conduction, a heterogeneous thermal field has be considered. Furthermore, in the context of large strains, the configuration for the laplacian term calculation has to be chosen. It is described here after.

4.3.1. Generation of the numerical visible and IR images

The visible images were obtained by numerically deforming a speckle image. The numerical deformation imposed is a homogeneous vertical stretch, which leads to a deformation gradient tensor equal

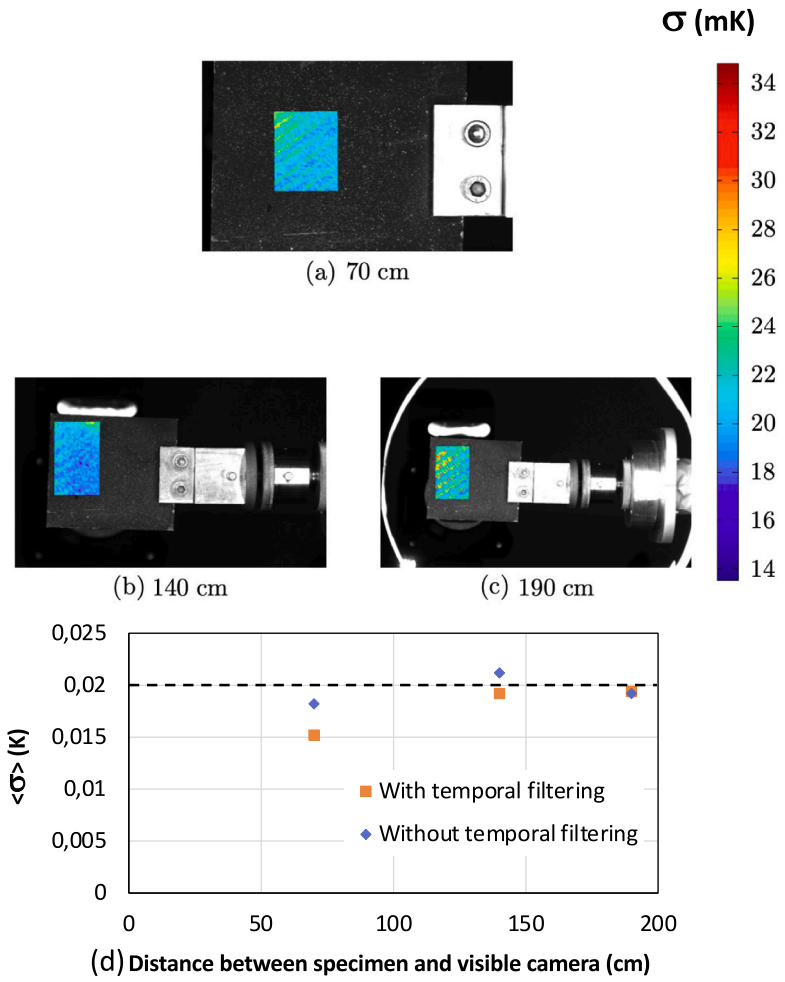

Fig. 11. Cartography of the standard deviation of the temperature variation obtained for several distance between the CCD camera and the specimen ((a) to (c)) (d) Mean standard deviation of the temperature variation versus the several distance between the CCD camera and the specimen, with and without temporal filtering (centered filter of size equal to 3).

to $\mathbf{F} = \begin{pmatrix} 1 & 0 \\ 0 & \lambda \end{pmatrix}$. The spatial resolution of the image is equal to 0.026 mm/px. Fig. 19 shows the images obtained at both the undeformed and deformed state. It could corresponds to out-of-plane pure shear in the case of an incompressible rubber-like material. This formulation is for the validation of the conduction term in the heat diffusion equation in a case as simple as possible.

The IR images were obtained by the same way. The spatial resolution of the image is equal to 0.15 mm/px. A temperature gradient is added to the image by using a Gaussian surface expressed as followed:

$$T(x,y) = A \exp \frac{(x-x_0)^2+(y-y_0)^2}{\omega} \tag{16}$$

with A represents the maximal temperature (in K), which is obtained at the position (x_0, y_0), and ω represents the spreading of the Gaussian surface (in mm). Knowing both the temperature and deformation field, the analytical solution can be calculated. Here, two situations are considered, $A = 5\ K$ and $\omega = 10$ mm, and $A = 1\ K$ and $\omega = 1$ mm, which is consistent with what can be found in the case of heterogeneous temperature fields studied in elastomers [27,28,43]. A numerical noise is added to the IR images obtained to better simulate data that can be obtained with an IR camera (see the noise characterization in the previous section). The corresponding temperature fields are given in Fig. 20. Fig. 21 shows the images obtained at both the undeformed (a and b) and deformed states (c and d).

4.3.2. Calculation of the heat conduction term

The large strains formalism requires choosing a configuration (Lagrangian ou Eulerian) for calculating the laplacian term. In function of the configuration chosen, the spatial resolution of temperature field may have a strong effect on the results, depending on the spatial temperature gradients involved. In this paper, we present the calculation of the heat conduction term in the Lagrangian configuration. In the case of incompressible materials and isotropic heat conduction, the heat influx per unit reference area (the Lagragian heat influx) writes $\mathrm{Q} = -k_0 \mathbf{C}^{-1} \mathrm{Grad}\, T$. The thermal conduction term has been numerically calculated from the noisy thermal fields. In parallel, the thermal conduction term is determined analytically from the exact expression the Gaussian surfaces. The difference between both results can be mapped in terms of the absolute error as illustrated in Fig. 22. It clearly appears that the singularity is not fully captured in the situation where $A = 1\ K$ and $\omega = 1$ mm. This can be an issue in the case where the measurement is performed at a crack tip in a rubber specimen.

Indeed, in the case of the Lagrangian calculation of the heat conduction term is carried out with respect to the undeformed state and therefore by tracking the temperature at points of the initial (undeformed) kinematic grid in the deformed state. Therefore, the spatial resolution of the thermal field is altered by increasing the strain level. To overcome this issue, an oversampling operation can be done, such as explained in Part II of the present paper.

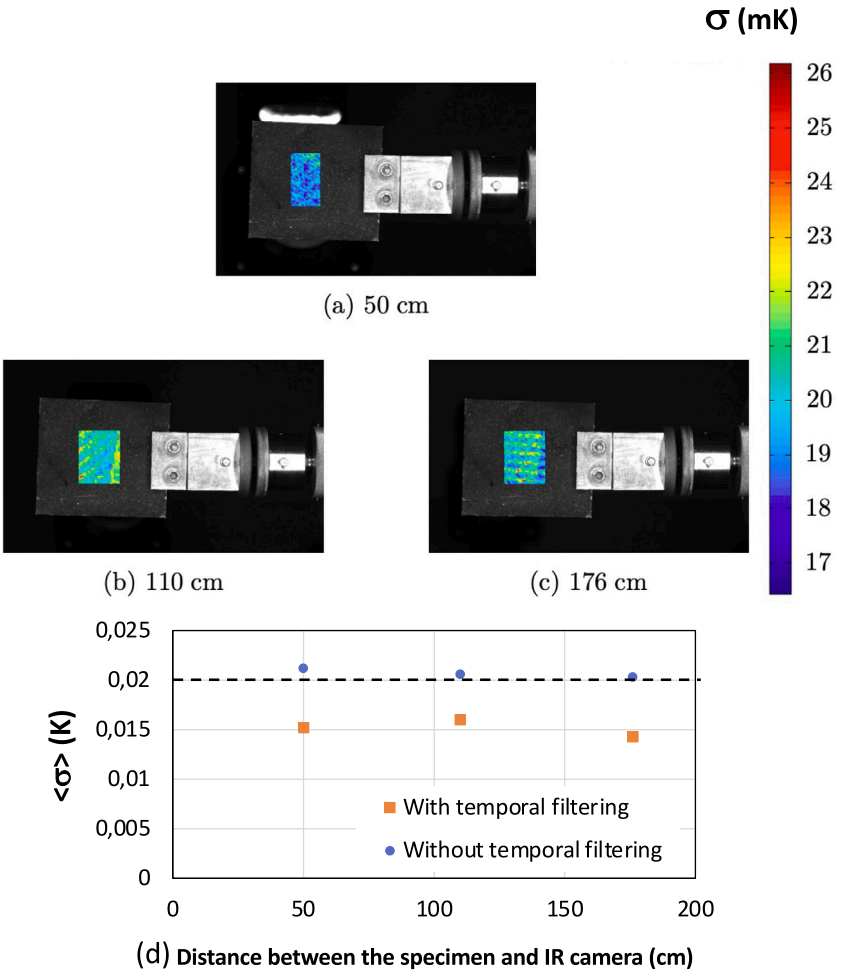

Fig. 12. Cartography of the standard deviation of the temperature variation obtained for several distance between the IR camera and the specimen ((a) to (c)) (d) Mean standard deviation of the temperature variation versus the several distance between the IR camera and the specimen, with and without temporal filtering (centered filter of size equal to 3).

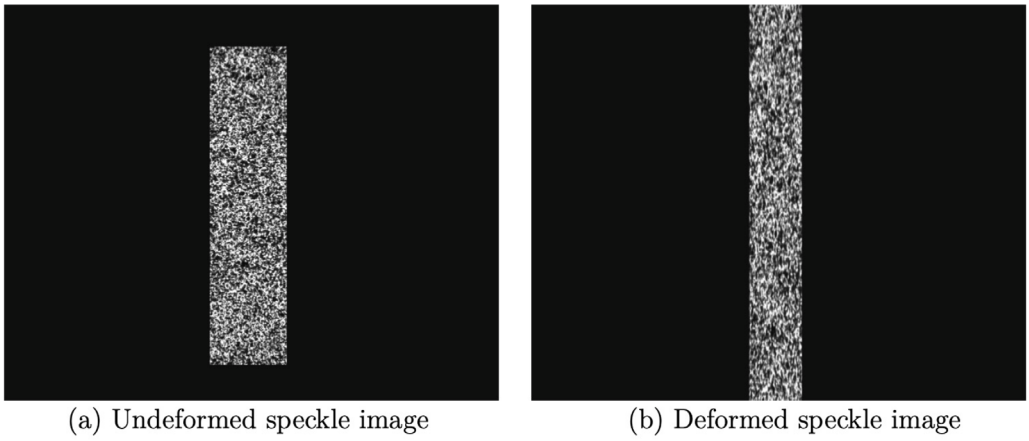

Fig. 13. Images of the speckle image in the undeformed (a) and maximum deformed (b) states.

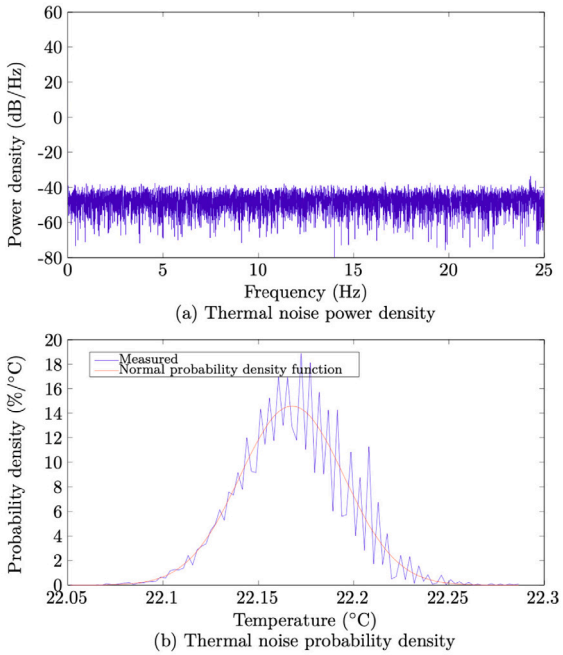

Fig. 14. Power density of thermal noise measured.

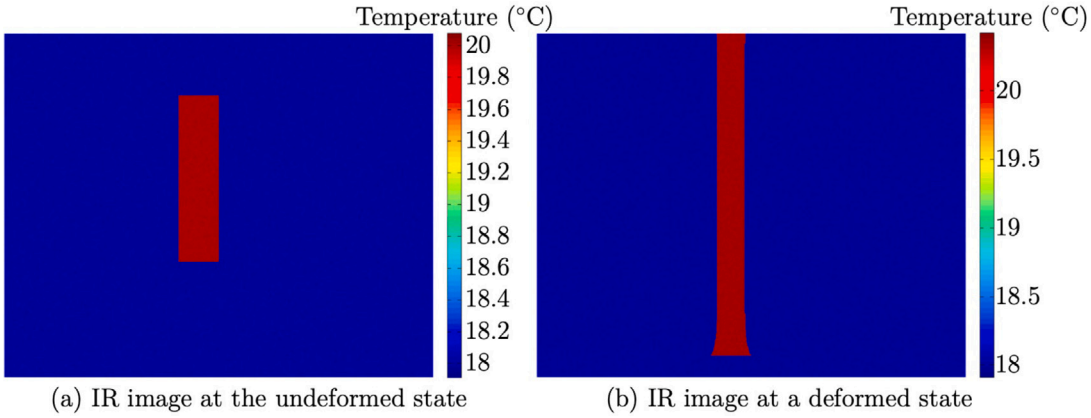

Fig. 15. IR images created.

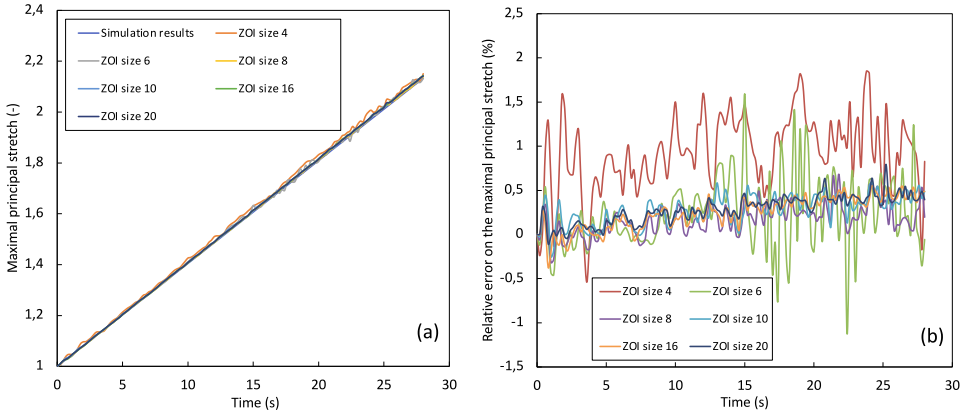

Fig. 16. Evolution of the maximal principal stretch for different ZOI sizes.

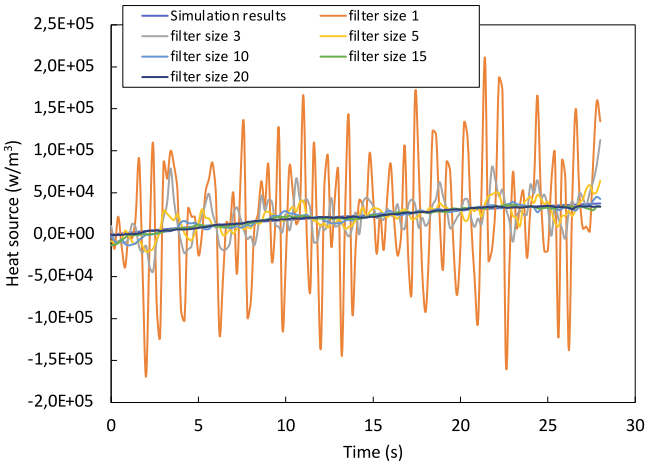

Fig. 17. Evolution of the heat source for different temporal filter sizes.

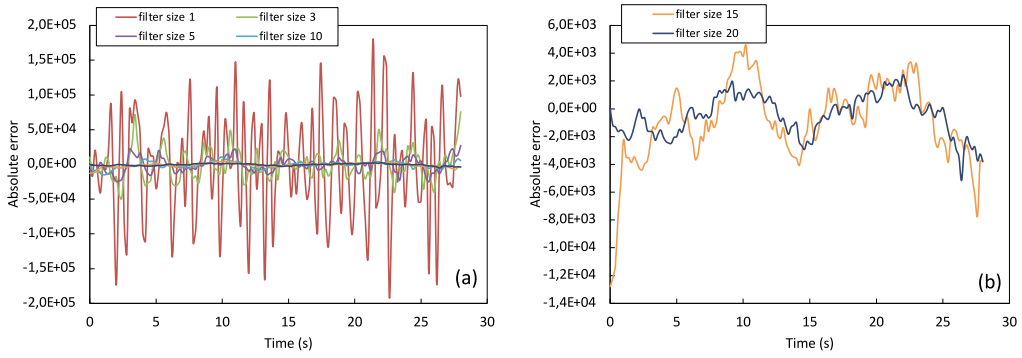

Fig. 18. Absolute error for the different temporal filter sizes.

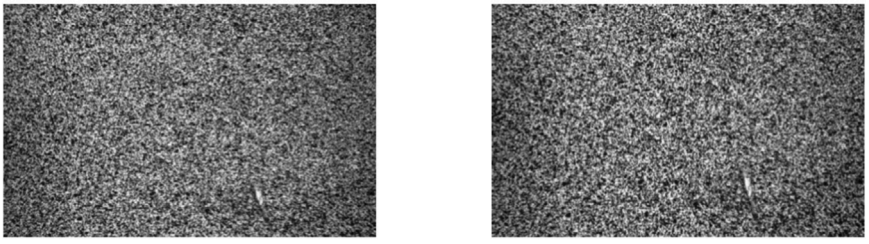

(a) Undeformed speckle image (b) Deformed speckle image

Fig. 19. CCD images obtained by the numerical deformation of a speckle.

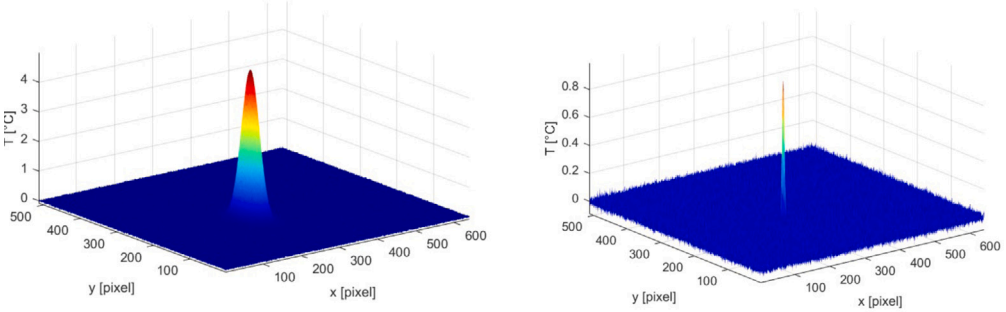

A = 5 °C, σ = 10 mm A = 1 °C, σ = 1 mm

Fig. 20. Noised numerical thermal field with two different gaussian surfaces.

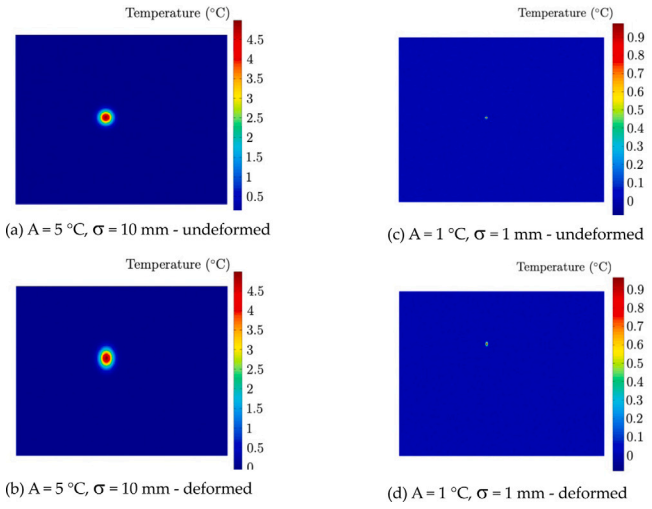

Fig. 21. IR images obtained by the numerical deformation of the noised gaussian temperature fields.

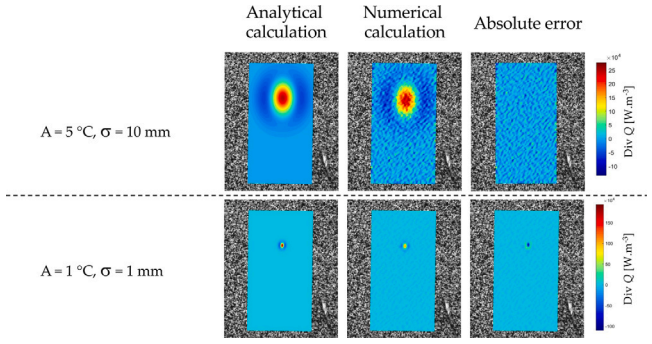

Fig. 22. Thermal conduction term fields: analytical solutions, the noised gaussian temperature fields and absolute errors.

5. Conclusion

In the present study, a methodology for reconstructing the heat source surface fields in the case of large heterogeneous deformations has been developed. This methodology is based on the coupling of kinematic and thermal measurements, post-processed by a method of compensating for the motion of points in the thermal images and the heat diffusion equation. Several results can be drawn:

- the compensation technique does not alter significantly the thermal resolution in the variation range of experimental parameters in relation with the experimental setup used,
- the heat source resolution without calculating the diffusion term can be 5 10^3 W/m^3 by increasing the temporal filtering of the temperature variation signal. This resolution is 2 orders of magnitude less than what is classically measured in elastomers. The methodology is therefore well suitable to characterize the calorimetric response of high strain gradient zones such as crack tip zones,
- the conduction term is accurately calculated in the Lagrangian configuration. An oversampling method can be used in the case of strong temperature gradients, this is addressed in Part II of the present paper.

In Part 2 of the present paper, the methodology proposed is used to determine full strain, calorimetric and strain-induced crystallinity fields at the crack tip of a natural rubber previously notched and subjected to cyclic loadings. As the value of the different parameters used for characterizing the crack tip behavior are in the range considered in the present part, the conclusions of the metrological analysis also apply to the measurements performed at the crack tip in part II.

CRediT authorship contribution statement

J. Trubert: Methodology, Investigation, Formal analysis, Data curation. **J.-B. Le Cam:** Writing – review & editing, Writing – original draft, Validation, Supervision, Resources, Project administration, Methodology, Conceptualization. **S. Charlès:** Validation, Supervision, Software, Methodology, Investigation, Formal analysis, Data curation, Conceptualization. **R. Fernandes:** Methodology, Formal analysis, Data curation. **V. Lemos:** Methodology, Formal analysis, Data curation.

Declaration of competing interest

The authors declare the following financial interests/personal relationships which may be considered as potential competing interests: The authors declare that they have no known competing financial interests or personal relationships that could have appeared to influence the work reported in this paper.

Acknowledgments

Dr E. Robin is acknowledged for providing the tracking point algorithm. Dr E. Robin, Dr M. Miroir, M. M. Le Fur and M. V. Burgaud are acknowledged for the development of the home-made biaxial testing machine. The authors acknowledge the “Manufacture Française des pneumatiques Michelin” for providing the specimens. Dr P. Vacher is acknowledged for providing the digital image correlation software 7D.

Data availability

Data will be made available on request.

References

[1] A. Chrysochoos, Energy-balance for elastic–plastic deformation at finite strain, J. Mec. Theo Appl. 4 (1985) 589–614.
[2] A. Chrysochoos, V. Huon, F. Jourdan, J. Muracciole, R. Peyroux, B. Wattrisse, Use of full-field digital image correlation and infrared thermography measurements for the thermomechanical analysis of material behaviour, Strain 46 (2010) 117–130.
[3] V. Honorat, S. Moreau, J. Muracciole, B. Wattrisse, A. Chrysochoos, Calorimetric analysis of polymer behaviour using a pixel calibration of an irfpa camera, Quant. Infrared Thermogr. 2 (2005) 189–200.
[4] R. Caborgan, Contribution à L’Analyse ExpÉrimentale Du Comportement ThermomÉcanique Du Caoutchouc Naturel Ph.D. thesis. Thèse de doctorat, 2011, Montpellier 2.
[5] J.R. Samaca Martinez, J.-B. Le Cam, X. Balandraud, E. Toussaint, J. Caillard, Thermal and calorimetric effects accompanying the deformation of natural rubber. part 2: quantitative calorimetric analysis, Polymer 54 (2013) 2727–2736.
[6] Le Cam J.-B., Energy storage due to strain-induced crystallization in natural rubber: the physical origin of the mechanical hysteresis, Polymer 127 (2017) 166–173.
[7] J.R. Samaca Martinez, J.-B. Le Cam, X. Balandraud, E. Toussaint, J. Caillard, Filler effects on the thermomechanical response of stretched rubbers, Polym. Test. 32 (2013) 835–841.
[8] J.R. Samaca Martinez, J.-B. Le Cam, X. Balandraud, E. Toussaint, J. Caillard, New elements concerning the mullins effect: A thermomechanical analysis, Eur. Polym. J. 55 (2014) 98–107.
[9] V. Khiem, J.-B. Le Cam, S. Charlès, M. Itskov, Thermodynamics of strain-induced crystallization in filled natural rubber under uni- and biaxial loadings. part i: complete energetic characterization and crystallinity evaluation, J. Mech. Phys. Solids 159 (2022) 104701.
[10] D. Göritz, F.H. Müller, Changes of state in ploymeric networks during orientation. ii. analysis of elongation-induced crystallization by calorimetry, Kolloid-Zeitschrift Und Z. Für Polym. 251 (892) (1973).
[11] Le Cam J.-B., Strain-induced crystallization in rubber: A new measurement technique, Strain 54 (2018) e12256.

[12] K. Vu Gnoc, J.-B. Le Cam, S. Charlès, M. Itskov, Thermodynamics of strain-induced crystallization in filled natural rubber under uni- and biaxial loadings. part ii: hhysically-based constitutive theory, J. Mech. Phys. Solids 159 (2022) 104712, Submitted to.
[13] A. Chrysochoos, H. Louche, An infrared image processing to analyse the calorific effects accompanying strain localisation, Internat. J. Engrg. Sci. 38 (2000) 1759–1788.
[14] A. Chrysochoos, H. Louche, Thermal and dissipative effects accompanying luders band propagation, Mat. Sci. Eng. A-Struct 307 (2001) 15–22.
[15] X. Balandraud, A. Chrysochoos, S. Leclercq, R. Peyroux, Influence of the thermomechanical coupling on the propagation of a phase change front, C R Acad Sci - Ser. IIB - Mech. 329 (2001) 621–626.
[16] A. Chrysochoos, B. Wattrisse, J. Muracciole, Y. El Kaim, Fields of stored energy associated with localized necking of steel, J. Mech. Mater. Struct. 4 (2009) 245–262.
[17] D. Delpueyo, X. Balandraud, M. Grédiac, Calorimetric signature of the Portevin-Â" Le Chatelier effect in an aluminum alloy from infrared thermography measurements and heat source reconstruction, Mater. Sci. Eng.: A - Struct. Mater. Prop. Microstruct. Process. 651 (2016) 135–145.
[18] J.-B. Le Cam, E. Robin, L. Leotoing, D. Guines, Calorimetric analysis of portevin-le chatelier bands under equibiaxial loading conditions in al–mg alloys: Kinematics and mechanical dissipation, Mech. Mater. 105 (2017) 80–88.
[19] L. Leotoing, D. Guines, E. Robin, J.-B. Le Cam, Effects of strain path changes on the kinematics and the intrinsic dissipation accompanying plc bands in al-mg alloys, Exp. Mech. 59 (2019) 963–977.
[20] V. Kerchman, C. Shaw, Experimental study and finite element simulation of heat build-up in rubber compounds with application to fracture, Rubber Chem. Technol. 76 (2003) 386–405.
[21] C. Liu, B. Gu, J. Chen, L. Zhang, Y. Lu, F. Li, Thermo-mechanical coupling analysis of edge-cracked rubber specimen focusing on the crack tip: Experimental observation and numerical simulation, Mater. Today Commun. 31 (2022) 103348.
[22] L. Meunier, G. Chagnon, D. Favier, L. Orgéas, P. Vacher, Experimental and numerical study of the mechanical behaviour of an unfilled silicone rubber, Polym. Test. 27 (2008) 765–777.
[23] J.-B. Le Cam, A review of the challenges and limitations of full-field measurements applied to large heterogeneous deformation of rubbers, Strain (2012) http://dx.doi.org/10.1111/j.1475-1305.2011.00830.x, To appear in.
[24] E. Toussaint, X. Balandraud, J.-B. Le Cam, M. Grédiac, Combining displacement, strain, temperature and heat source fields to investigate the thermomechanical response of an elastomeric specimen subjected to large deformations, Polym. Test. 31 (2012) 916–925.
[25] S. Charlès, J.-B. Le Cam, Inverse identification from heat source fields: a local approach applied to hyperelasticity, Strain (2020) e12334, http://dx.doi.org/10.1111/str.12334.
[26] D. Nozaki, T.-T. Mai, K. Tsunoda, K. Urayama, Tracking the evolution of heterogeneous crystallization driven by complex deformation scenarios in natural rubber, Macromolecules 58 (2025) 4059–4069.
[27] J. Samaca Martinez, X. Balandraud, E. Toussaint, J.-B. Le Cam, D. Berghezan, Thermomechanical analysis of the crack tip zone in stretched crystallizable natural rubber by using infrared thermography and digital image correlation, Polymer 55 (2014) 6345–6353.
[28] J.R. Samaca Martinez, E. Toussaint, X. Balandraud, J.-B. Le Cam, D. Berghezan, Heat and strain measurements at the crack tip of filled rubber under cyclic loadings using full-field techniques, Mech. Mater. 81 (2015) 62–71.
[29] A. Chrysochoos, Analyse du comportement des matériaux par thermographie infra rouge, in: Colloque PhotomÉcanique, vol. 95, 1995, pp. 201–211.
[30] H. Louche, Etudes de certains phénomènes de localisation à partir de champs thermomécaniques Habilitation thesis, Savoie University, 2009.
[31] E. Verron, A. Andriyana, Definition of a new predictor for multiaxial fatigue crack nucleation in rubber, J. Mech. Phys. Solids 56 (2008) 417–443.
[32] H. Baaser, C. Hopmann, A. Schobel, Reformulation of strain invariants at incompressibility, Arch. Appl. Mech. 83 (2013) 273–280.
[33] L. Bodelot, Etude du couplage de champs cinématiques et thermiques à l'échelle de la microstructure des matériaux métalliques Phd thesis, Université de Lille, 2008.
[34] L. Bodelot, L. Sabatier, E. Charkaluk, P. Dufrénoy, Experimental setup for fully coupled kinematic and thermal measurements at the microstructure scale of an AISI 316L steel, Mater. Sci. Eng.: A 501 (2009) 52–60.
[35] T. Pottier, M.-P. Moutrille, J.-B. Le Cam, X. Balandraud, M. Grédiac, Study on the use of motion compensation technique to determine heat sources, application to large deformations on cracked rubber specimens, Exp. Mech. 49 (2009) 561–574.
[36] J.-B. Le Cam, E. Toussaint, The mechanism of fatigue crack growth in rubbers under severe loading: the effect of stress-induced crystallization, Macromolecules 43 (2010) 4708–4714.
[37] P. Vacher, S. Dumoulin, F. Morestin, S. Mguil-Touchal, Bidimensional strain measurement using digital images. Proceedings of the institution of mechanical engineers, Part C: J. Mech. Eng. Sci. (1999) 213.
[38] E. Jones, M. Iadicola, A Good Practices Guide for Digital Image Correlation, International Digital Image Correlation Society, 2018.
[39] L.R.G. Treloar, The elasticity and related properties of rubbers, Rep. Progr. Phys. 36 (755) (1973).
[40] X. Balandraud, J.B. Le Cam, Some specific features and consequences of the thermal response of rubber under cyclic mechanical loading, Arch. Appl. Mech. 84 (2014) 773–788.
[41] A. Lachhab, E. Robin, J.-B. Le Cam, F. Mortier, Y. Tirel, F. Canevet, Energy stored during deformation of crystallizing tpu foams, Strain (2018) e12271.
[42] R.W. Schafer, What is a savitzky-golay filter? [lecture notes], in: IEEE Signal Processing Magazine, vol. 28, IEEE, 2011, pp. 111–117.
[43] C. Liu, B. Gu, J. Chen, L. Zhang, Y. Lu, F. Li, Thermo-mechanical coupling analysis of edge-cracked rubber specimen focusing on the crack tip: Experimental observation and numerical simulation, Mater. Today Commun. 31 (2022) 103348.